ISSN (Print) 1226-1750
ISSN (Online) 2233-6656
Journal of Magnetics 31(3), 424-437 (2026) https://doi.org/10.4283/JMAG.2026.31.3.424

Comparative Study of Magnetized Casson and Casson-Maxwell Nanofluid across Stretchable Spinning Disks

Yasir Khan[1], Arfan Shahzad[2], Arshad Riaz[3]*, Safia Akram[4], and A. Alameer[1]

[1]*Department of Mathematics, College of Science, University of Hafr Al-Batin, Hafr Al-Batin, Saudi Arabia*
[2]*Department of Sciences & Humanities, National University of Computer and Emerging Sciences, Chiniot-Faisalabad Campus 38000, Pakistan*
[3]*Department of Mathematics, Division of Science and Technology, University of Education, Lahore 54770, Pakistan*
[4]*MCS, National University of Sciences and Technology, Islamabad, Pakistan*

(Received 6 June 2026, Received in final form 31 July 2026, Accepted 5 August 2026)

A steady, incompressible, and electrically conductive Casson-Maxwell nanofluid flow incorporating gyrotactic motile microbes is analyzed. The flow under a transverse magnetic field and chemical reaction is confined in two coaxial, parallel, and stretchable spinning disks. The Buongiorno model incorporates Brownian motion and thermophoresis. Similarity transformations convert the flow governing equations into ODEs and subsequently solved numerically using the bvp4c and the fourth-order RK technique to analyze the significance of the governing dimensionless parameters. The results confirmed that bioconvection promotes convective heat transfer by fluid mixing. The Lorentz force strongly suppresses the Casson-Maxwell fluid velocity. Increasing the Casson fluid parameter lowers the fluid velocity by stronger yield stress and effective viscosity. The stretching ratio boosts the flow, improving momentum transfer within the boundary layer. The concentration profile accelerates with thermophoresis but decelerates for chemical reaction and Brownian motion effects. The magnetic effect maximizes the microbes' density profile.

Keywords : bioconvection, Casson-maxwell nanofluid, Cattaneo-christov double diffusion theory, magnetohydrodynamics (MHD), magnetic field, stretchable disks

1. Introduction

The study of slip flow of bioconvective, radiative, and magnetized Casson–Maxwell nanofluids over stretchable spinning disks has significant applications in various advanced engineering and biomedical systems. Such flows are particularly relevant in the modeling of biofluids, including blood, where non-Newtonian characteristics and microorganism-induced bioconvection play a crucial role in transport phenomena. The inclusion of magnetic field effects makes the model applicable to magnetohydrodynamic (MHD) devices, biomedical treatments such as targeted drug delivery and hyperthermia, and metallurgical processes involving electrically conducting fluids. Moreover, rotating disk configurations are widely encountered in turbines, chemical reactors, and cooling systems for rotating machinery. The consideration of thermal radiation and internal heat generation enhances the applicability of the model in high-temperature systems, heat exchangers, and electronic cooling technologies. Additionally, the incorporation of chemical reaction effects is important in industrial processes such as polymer production, catalytic reactions, and coating flows. The presence of slip boundary conditions further extends the relevance of this study to micro and nanoscale systems, including microfluidic devices and MEMS/NEMS applications, where classical no-slip assumptions are no longer valid. Therefore, the present investigation provides a comprehensive framework for understanding complex fluid behavior in modern technological and industrial applications.

The role of non-Newtonian fluids is crucial in an extensive range of commercial fluids including plastics, wire coating, printing, engine oil (EO), polymers, glycerin, toothpaste, pulps, and fossil fluids. Several non-Newtonian models (Cross-fluid, Carreau fluid, rate-type fluid) have been proposed to simulate the inspection of these liquids. Considering the nonlinear existence of these fluids, shear

©The Korean Magnetics Society. All rights reserved.
*Corresponding author: Tel: +92-304-1415304
E-mail: arshad-riaz@ue.edu.pk

© 2026 Journal of Magnetics

rate and shear stress are associated with non-Newtonian fluids. For these types of fluids, the momentum equation includes dynamic nonlinear factors, making the problem more difficult to tackle. The Maxwell fluid is a non-Newtonian (rate type) viscoelastic. Rate-type models are more realistic than experimentation, considering they interpret both memory and elastic impacts [1]. Researchers have been interested in the flow between stretching surfaces because of its uses in industry, such as the extrusion of paper production and polymer sheets, and steel and plastic manufacturing. Because of the myriad industrial and technological applications, the problem of fluid flow across parallel discs is very crucial. These applications also cover manufacturing processes of semiconductors with rotating wafers, turbine engines, rotating machinery, hydro-dynamical machines and apparatus, crystal growth processes, biomechanics, computer storage devices, geophysical, geothermal, heat and mass exchanges, lubrication, oceanography, radial diffusers, etc.

The Casson-Maxwell fluid models have been used in several investigations. Shehzad *et al*. [2] interpreted the Casson fluid stream while assuming the radiation effect. Khan *et al*. [3] examined the outcomes of chemical reactions on the Casson fluid stream through a stretchable surface. Farooq *et al*. [4] implemented the phenomenon of porous media to examine a 2-dimensional Casson fluid flow. The attribution of entropy generation in the boundary layer of the Casson fluid stream was studied by Sohail and Shah [5]. Rashid *et al*. [6] discussed the Maxwell liquid flow across a stretchy surface incorporating Arrhenius activation energy. Khan *et al*. [7] portrayed an investigation on the effectiveness of Maxwell nanofluid stream through a spinning disk incorporating chemical reactions. For assessing the thermophoretic motion, Shehzad *et al*. [8] applied Fourier's law generalized theory to the magnetized Maxwell fluid stream. The consequences of bioconvective non-Newtonian Maxwell fluid flow induced by a spinning cylinder were outlined by Waqas *et al*. [9]. Gowda *et al.* [10] studied the deposition of thermophoretic particles on a hybrid nanofluid flow passing over a rotating disk that expands and contracts. Jayadevamurthy *et al*. [11] examined the hybrid fluid flow through spinning disks under chemical reactions and bioconvection. The MHD fluid flow by a stretching disk was elucidated by Turkyilmazoglu [12]. Ahmed *et al*. [13] revealed a flow analysis of the Maxwell fluid across the dual stretchable spinning disks.

Heat is a type of energy that can be transferred to a region of reduced concentration. Transformation sources of heat include radiation, conduction, and convection, with numerous applications in several manufacturing and industrial processes, like heating phenomena, cooling chambers, engines, and drying processes. Nanotechnology makes a significant contribution to meet the increasing demands of energy and responding to energy concerns currently. The suspension of nanomaterials in a base fluid productively increases its thermal transmission rate, including the thermal properties. The nanoparticles are used extensively in many applications related to heat exchangers, cooling transformers, electronic devices' cooling systems, nuclear reactors, space cooling systems, and cancer therapy. Choi [14] is the first one who presented the terminology "nanofluid", and he considered it for cooling purposes in different technologies. According to Buongiorno [15], Brownian movement and thermophoretic mechanisms have a key influence in upgrading the thermal aspects of the base fluid. Turkyilmazolglu [16] used an analytical approach to conclude the transport of heat and flow from momentum and energy equations of flow. Pourmehran [17] considered Al_2O_3 and Cu nanomaterials to monitor the mass and heat transmission in microchannels. Hatami *et al*. [18] investigated the thermal transmission in nano-liquids incorporating natural convection. Nadeem *et al*. [19] reported the Oldroyd-B fluid containing nanomaterials through a stretching sheet surface. Aziz and Afify [20] studied non-Newtonian nanofluids using the Lie group approach. Yang *et al*. [21] used Buongiorno Models for nanofluids to investigate the convective heat transfer in the concentric annulus.

There are several applications for fluid flow with wall slip conditions. The fluid flow problems with no-slip conditions have already been investigated enormously. Furthermore, the use of slip conditions in the flows has specific implications in biology and polymers. Hence, several studies associated with various fluids under slip constraints have been carried out. Hayat *et al*. [22] highlighted the features of double stratification fluid flow when the slip boundary constraints deployed to the magnetohydrodynamic nanofluid stream. The magnetohydrodynamic stream of Williamson fluid with Cattaneo-Christov's double diffusion and slip constraint was analyzed by Khan *et al.* [23]. The entropy causing in magnetohydrodynamic nanofluid with slip constraints was assessed by Qayyum *et al.* [24]. The impression of Cattaneo-Christov thermal flow rate intensity on a 2D nanofluid stream along with velocity slip was studied by Reddy *et al.* [25].

The macroscopic convection movement of fluids created by a density gradient due to the directional collective swimming of motile microbes is referred to as bioconvection. These microbes are multicellular organisms that can be found in animals, humans, and plants, and are classified as gyrotactic, oxytactic, gravitactic, or chemotactic, subject on the cause of their movement. Bioconvection is yet another intriguing research topic of bioengineering and physical science, and

is found in multiple domains, including biological polymer synthesis, the pharmaceutical industry, biosensors, biotechnology, water treatment plants, microbial improved oil recovery, purified cultures, and sustainable fuel cell-related technologies. Suspension of microorganisms in nanofluids can be utilized to provide stability to improve thermal transportation. The introductory work based on nanoparticle bioconvection was outlined by Kuznetsov [26]. Khan *et al.* [27] highlighted the relevance of bioconvection in the field of bioengineering by unveiling the investigation of the unsteady flow of Eyring-Powell nanofluid with different thermal characteristics. Chu *et al.* [28] discussed the Maxwell nanofluid over a 2-directional accelerated surface together with gyrotactic microbes and the heat creation. Khan *et al.* [29] examined the benefaction of slip causes in Oldroyd-B nanofluid in existence of gyrotactic microbes. Ramzan *et al.* [30] visualized the chemical reaction impacts for the magnetized and radiative nanofluid flow accommodating motile microorganisms. Shehzad *et al*. [31] employed the modified flow rate relations to investigate the crucial bioconvection phenomenon for micropolar nanofluids. Zohra *et al*. [32] investigated the thermal properties of water-based nanomaterial in the existence of motile microbes incorporating multiple slip conditions and Stefan blowing properties. Khan *et al.* [33] addressed how to use radiative phenomena and activation energy to outline the bioconvective attributes in the flow of micropolar nanoparticles restricted by the spinning disk. Nadeem *et al.* [34] analyzed the thermal efficiency of ferromagnetic nanomaterials with magnetic dipole and motile microbes. Ramachandru *et al.* [35] investigated the role of bioconvection and activation energy on MHD flow of Maxwell's nanofluid with gyrotactic microorganisms in porous media. Uddin *et al.* [36] examined the particle swarm optimization for exploring Darcy-Forchheimer flow of Casson fluid between co-axial rotating disks with the Cattaneo-Christov model. Beg *et al.* [37] addressed the CFD simulation of the aqueous humour in healthy or glaucomatous conditions. Bhatti [38] explored the numerical simulation and visualization of Newtonian and non-Newtonian hemodynamics in a stenotic blood vessel. Some relevant studies are also presented in [39-44].

The determination of this analysis is to traverse a three-dimensional, steady, incompressible, and electrically conductive Casson-Maxwell nanofluid flow accommodating gyrotactic motile microorganisms. The Buongiorno fluid model is implemented to scrutinize the Brownian motion and thermophoretic aspects. The contribution of microorganisms is analyzed through the bioconvection phenomena, which provide strength to thermal transportation. This study also explores the features of multiple slip constraints on the non-Newtonian fluid flow. The similarity transformations are employed to manage the fundamental equations of partial differentials to non-dimensional equations of ordinary differentials. These transformed ODEs, along with the boundary constraints, are approximated using the bvp4c solver and the RK4 method.

2. Mathematical Formulation of the Flow

A three-dimensional incompressible, steady, and electrically conductive Casson-Maxwell nanofluid flow accommodating gyrotactic motile microorganisms is assumed. Bioconvection is used to accommodate the contribution of gyrotactic motile microbes. To analyze the thermophoretic and Brownian motion effects, the Buongiorno model is applied to this non-Newtonian nanofluid stream. The fluid flow against a transverse magnetic field is confined in two coaxial, parallel, and stretchable disks apart a finite distance $2h$. Also, the governing equations of the flow model compiling the significance of thermal radiation and a heat source to the energy Eq. (7), and chemical reaction consequences to the concentration Eq. (8), are assumed. The bioconvection of motile microorganisms is modeled in Eq. (9). The upper and lower disks are considered fixed at positions $z = h$ and $z = -h$ with stretching rates of s_2 and s_1, respectively. The impressions along the tangential axis are ignored as the fluid flow is axisymmetric. The magnetic field induced is also ignored against extremely low magnetic Reynolds numbers. Assume (r, ϑ, z) the cylindrical coordinates, $\hat{V} = (u, v, w)$ a velocity field. The concentration

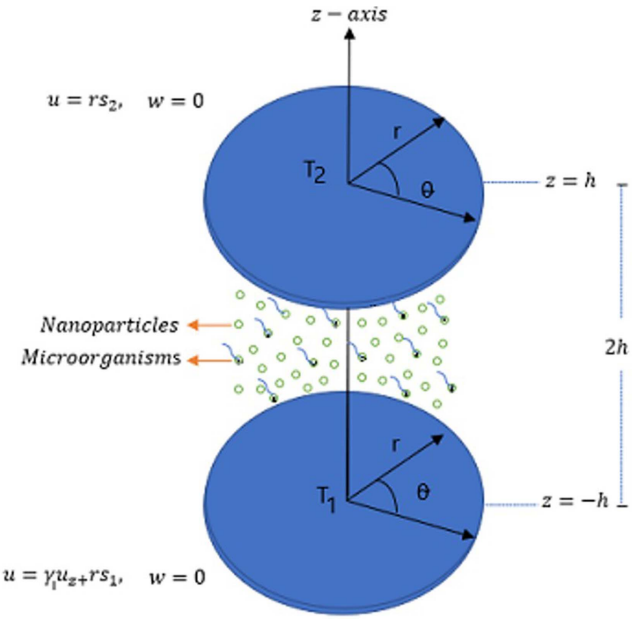


Fig. 1. (Color online) The flow model geometry.

of nanoparticles, temperature of nanofluid, and gyrotactic microorganisms' density at the top and bottom disks are denoted by (C_2, T_2, N_2) and (C_1, T_1, N_1), respectively. Fig. 1 depicts the flow model geometry.

For an incompressible Casson fluid stream, the rheological expression imparted as [45]:

$$\hat{\tau}_{ij} = \begin{cases} 2\left(\sqrt{2\pi} + \hat{\tau}_z/\mu_\beta\right)\tilde{e}_{ij}\,\pi_c < \pi, \\ 2\left(\sqrt{2\pi} + \hat{\tau}_z/\mu_\beta\right)\tilde{e}_{ij}\,\pi_c > \pi \end{cases} \tag{1}$$

where $\pi_c, \tilde{e}_{ij}, \pi = \tilde{e}_{ij}\,\tilde{e}_{ij}, \hat{\tau}_z$ and μ_β denote the critical values based on the product of the non-Newtonian fluid model, rate of deformation, the product of deformation rate component by itself, plastic dynamic viscosity, and yield stress, respectively.

The fundamental equation for the Maxwell fluid is [46]:

$$\rho(\nabla \cdot V)V = \nabla \cdot \tilde{S} - \nabla p + \tilde{J} \times \tilde{B} \tag{2}$$

Here $\rho, p, \hat{V}, \tilde{S}, \tilde{J},$ and $\tilde{B}$ determine the density of fluid, pressure, velocity vector, stress tensor of Maxwell fluid, current density, and magnetic field, respectively. The stress tensor of Maxwell fluid can be computed from the expression $\tilde{S} = \dfrac{\mu A_1}{1 + \lambda_1 D/Dt}$, where μ, A_1, λ and D/Dt represents the dynamic viscosity, relaxation time, first tensor of Rivlin-Ericksen, and upper convected material derivative that is given by the expression

$$\frac{D}{Dt}\left(\tilde{S}\right) = \left(\nabla.\hat{V}\right)\tilde{S} + \frac{\partial \tilde{S}}{\partial t} - \tilde{S}\left(L + L'\right), \text{ where } L = grad\left(V\right). \tag{3}$$

Based on presumptions, the fundamental equations of the flow are [46-48]:

$$u_r + \frac{u}{r} + w_z = 0\,, \tag{4}$$

$$\begin{aligned} &uu_r + wu_z - \frac{u^2}{r} = -\frac{1}{\rho}\partial_r(p) + \nu\left(1 + \frac{1}{\beta}\right)\left(2u_{rr} + u_{zz} + w_{zr} + \frac{2}{r}u_r - \frac{2u}{r^2}\right) \\ &-\lambda_1\begin{pmatrix} u^2u_{rr} + w^2u_{zz} \\ +2uwu_{zr} \end{pmatrix} - \frac{\sigma_e\beta_0^2}{\rho}\left(u + \lambda_1 wu_z\right) \\ &+\frac{g}{\rho_f}\begin{bmatrix} \beta^{**}\rho_f\left(T - T_2\right)\left(1 - C_f\right) + \left(\rho_f - \rho_p\right)\left(C - C_2\right) + \gamma^*\left(\rho_f - \rho_m\right) \\ \left(N - N_2\right) \end{bmatrix}, \end{aligned} \tag{5}$$

$$\begin{aligned} &uw_r + ww_z = -\frac{1}{\rho}\partial_r(p) + \nu\left(1 + \frac{1}{\beta}\right)\left(w_{rr} + 2w_{zz} + u_{zr} + \frac{1}{r}u_z + \frac{1}{r}w_r\right) \\ &-\lambda_1\begin{pmatrix} u^2w_{rr} + w^2w_{zz} \\ +2uww_{zr} + \dfrac{\nu^2}{r}w_r \end{pmatrix}, \end{aligned} \tag{6}$$

$$\begin{aligned} &\left(uT_r + wT_z\right) = \frac{k}{\rho c_p}\left(T_{rr} + \frac{1}{r}T_r + T_{zz}\right) \\ &-\tau\left(D_B\left(C_rT_r + C_zT_z\right) + \frac{D_T}{T_m}\left(\left(T_r\right)^2 + \left(T_z\right)^2\right)\right) \\ &-\tau_1\begin{pmatrix} uu_rT_r + ww_zT_z + uw_rT_z + wu_zT_z \\ +2uwT_{zr} + u^2T_{rr} + w^2T_{zz} \end{pmatrix} \\ &+\frac{Q}{\left(\rho c_p\right)_f}\left(T - T_2\right) - \frac{1}{\left(\rho c_p\right)_f}\partial_z\left(q_r\right), \end{aligned} \tag{7}$$

$$\begin{aligned} &uC_r + wC_z = D_B\left(C_{rr} + \frac{1}{r}C_r + C_{zz}\right) + \frac{D_T}{T_m}\left(T_{rr} + \frac{1}{r}T_r + T_{zz}\right) \\ &-\tau_2\begin{pmatrix} uu_rC_r + ww_zC_z + uw_rC_z \\ +wu_zC_r + 2uwC_{zr} + u^2C_{rr} \\ +w^2C_{zz} \end{pmatrix} + K_r^*\left(C - C_2\right), \end{aligned} \tag{8}$$

$$\begin{aligned} &uN_r + wN_z = D_n\left(\frac{1}{r}N_r + N_{rr} + N_{zz}\right) - \frac{bWc}{\left(C_1 - C_2\right)} \\ &\left(C_zN_z - C_{zz}N\right), \end{aligned} \tag{9}$$

According to the nonlinear thermal radiation Rosseland's approximation [49], the net radiative heat flow is given as:

$$q_r = -\frac{4\sigma^*}{3k^*}\left(\partial_z T^4\right) = -\frac{16\sigma^*}{3k^*}T^3\left(\partial_z T\right) \tag{10}$$

$$\partial_y\left(q_r\right) = -\frac{16\sigma^*}{3k^*}T^3\left(\partial_{zz}T\right) - \frac{16\sigma^*}{3k^*}T^2\left(\partial_z T\right)^2 \tag{11}$$

Implementing on energy Eq. (7) leads to

$$\begin{aligned} &\left(uT_r + wT_z\right) = \frac{k}{\rho c_p}\left(T_{rr} + \frac{1}{r}T_r + T_{zz}\right) \\ &-\tau\left(D_B\left(C_rT_r + C_zT_z\right) + \frac{D_T}{T_m}\left(\left(T_r\right)^2 + \left(T_z\right)^2\right)\right) \\ &-\tau_1\begin{pmatrix} uu_rT_r + ww_zT_z + uw_rT_z + wu_zT_z \\ +2uwT_{zr} + u^2T_{rr} + w^2T_{zz} \end{pmatrix} + \frac{Q}{\left(\rho c_p\right)_f}\left(T - T_2\right) \\ &+\frac{16\sigma^*T^3}{3k^*\left(\rho c\right)_p}T_{zz}, \end{aligned} \tag{12}$$

The assumed boundary limitations for the flow model under discussion are [5,50]:

$$\begin{cases} u = \tilde{\gamma}_1u_z + rs_1, w = 0,\ T = \tilde{\gamma}_2T_z + T_1,\ C \\ \quad = \tilde{\gamma}_3C_z + C_1,\ N = \tilde{\gamma}_4N_z + N_1, \quad at\ z = -h \\ u = rs_2,\ w = 0,\ T - T_2 =,\ C - C_2 = 0,\ N - N_2 = 0, \\ \qquad\qquad at\ z = h. \end{cases} \tag{13}$$

Here (u, v, w) the velocity components, (u_r, w_z) etc. the partial derivatives of velocity components w.r.t "r" and "z", respectively, ν the kinematic viscosity, ρ_f the fluids' density, ρ_p the nanoparticles' concentration, ρ_m the microorganisms' density, $(\rho c_p)_f$ the base fluid heat capacity, $\boldsymbol{r}$ the radius of disk, g the gravity, p the pressure, c_p the specific heat, k the thermal conductivity, k^* the mean absorption coefficient, λ_1 the time relaxation, β the Casson fluid parameter, β_0 the magnetic field strength, β^{**} the coefficient of thermal expansion, σ_e the electrical conductivity, σ^* the Stefan-Boltzmann constant, τ the nanoparticles' heat capacity and base fluid ratio, τ_1 the heat flow rate relaxation time, τ_2 the mass flow rate relaxation time, γ^* the average volume for the microorganism, γ_1 the coefficient of velocity slip, γ_2 the thermal slip coefficient, γ_3 the centration slip, γ_4 the microorganisms slip coefficient, K_r^* the reaction rate constant, Q^* the heat source, D_B the Brownian diffusion parameter, D_T the thermophoretic diffusion parameter, D_n the microbes diffusion coefficient, Wc the maximum swimming speed of microbes, and T_m the mean temperature, respectively.

2.1. Similarity Transformation Functions

The suitable similarity transformation functions [51] are used to convert PDEs (5,6,8,9,12) to a dimensionless form of ordinary differential equations.

$$\begin{cases} u=-\dfrac{rs_1}{2}F'(\zeta),\ w=hs_1F(\zeta),\ \theta(\zeta)=\dfrac{T-T_2}{T_1-T_2}, \\ \phi(\zeta)=\dfrac{C-C_2}{C_1-C_2},\ \chi(\zeta)=\dfrac{N-N_2}{N_1-N_2},\ where\ \zeta=\dfrac{z}{h}. \end{cases} \tag{14}$$

The equation of continuity (4) is verified under (14), and transformed dimensionless equations after elimination of the pressure term, we have

$$\begin{aligned} &(1+1/\beta)F^{(iv)}-\mathrm{Re}\left(FF'''+M^2F''\right) \\ &-De\,\mathrm{Re}\left(F^2F^{(iv)}+\left(F'+M^2\right)FF'''\right. \\ &\left.-F'F''\left(F'-M^2\right)-FF''^2\right)+\lambda(\theta-Nr\phi-Nc\chi)=0, \end{aligned} \tag{15}$$

$$\begin{aligned} &\theta''\left(2+\frac{4}{3}Rd\right)-\mathrm{Pr}\,\mathrm{Re}\,\lambda_2\left(F^2\theta''+FF'\theta'\right) \\ &-\mathrm{Pr}\left(\mathrm{Re}\,F\theta'-Nb\theta'\phi'-Nt\theta'^2-Q\theta\right)=0, \end{aligned} \tag{16}$$

$$\begin{aligned} &\phi''-Sc\left(\mathrm{Re}\,\lambda_3\left(F^2\phi''+FF'\phi'\right)+\mathrm{Re}\,F\phi'\right) \\ &-\mathrm{Pr}\,LeKc\phi+\frac{Nt}{Nb}\theta''=0, \end{aligned} \tag{17}$$

$$\chi''-\chi'\left(LbRef+Pe\phi'\right)-Pe\phi''\left(\chi+N_\delta\right)=0 \tag{18}$$

with transformed boundary limitations

$$\left.\begin{aligned} &F'(-1)=\alpha_1F''(-1)+2,F(-1)=0, \\ &\theta(-1)=\alpha_2\theta'(-1)+1,\phi(-1)=\alpha_3\phi'(-1)+1, \\ &\chi(-1)=\alpha_4\chi'(-1)+1 \\ &\& \\ &F'(1)=-2\alpha_1,F(1)=0,\theta(1)=0,\phi(1)=0, \\ &\chi(1)=0. \end{aligned}\right\} \tag{19}$$

The main engineering quantities to measure the heat, mass, and motile microbes' fluxes, namely the local Nusselt, Sherwood, and the density numbers of microbes, respectively, at both disks are described as [52]:

$$\left.\begin{aligned} &Nu_{(-1).r}=-\theta' \\ &Sh_{(-1).r}=-\phi' \\ &Sn_{(-1).r}=-\chi' \end{aligned}\right|_{\zeta=-1},\quad \left.\begin{aligned} &Nu_{(1).r}=-\theta' \\ &Sh_{(1).r}=-\phi' \\ &Sn_{(1).r}=-\chi' \end{aligned}\right|_{\zeta=1} \tag{20}$$

3. Numerical Scheme

In the current study, a BVP4C and the fourth-order RK technique are adopted to solve the transformed nonlinear ODEs (15-18) according to the boundary constraints (19). The graphical and numerical findings show the consequences of flow constraints on velocity, temperature, concentration, and the microorganisms' concentration profiles. For this purpose, first, we lessen the order of these equations by establishing a few supplementary variables as

$$\left.\begin{aligned} &F^{(iv)}=P_4',F'''=P_4,F''=P_3,F'=P_2,F=P_1, \\ &\theta''=P_6',\theta'=P_6,\theta=P_5, \\ &\phi''=P_8',\phi'=P_8,\phi=P_7, \\ &\chi''=P_{10}',\chi'=P_{10},\chi=P_9 \end{aligned}\right\} \tag{21}$$

We get the following:

$$\begin{aligned} P_4'=&\frac{1}{\left(1+1/\beta-De\,\mathrm{Re}\,P_1^2\right)} \\ &\left[\begin{aligned} &+\mathrm{Re}\,P_1P_4+M^2\,\mathrm{Re}\,P_3+De\,\mathrm{Re}\left(P_1P_4\left(M^2+P_2\right)\right. \\ &\left.+P_2P_3\left(M^2-P_2\right)-P_1P_3^2\right)-\lambda(P_5-NrP_7-NcP_9) \end{aligned}\right], \end{aligned} \tag{22}$$

$$\begin{aligned} P_6'=&\frac{1}{\left(2+\dfrac{4}{3}Rd+\mathrm{Pr}\,\mathrm{Re}\,\lambda_2P_1^2\right)} \\ &\left[\mathrm{Pr}\,\mathrm{Re}\,\lambda_2\left(P_1P_2P_6\right)+\mathrm{Pr}\left(\mathrm{Re}\,P_1P_6-NbP_6P_8-NtP_6^2-SP_5\right)\right], \end{aligned} \tag{23}$$

$$P_8^{'}=\frac{1}{\left(1-Sc\,\mathrm{Re}\,\lambda_3F^2\right)}\left[Sc\left(\mathrm{Re}\,\lambda_3\left(P_1P_2P_8\right)+\mathrm{Re}\,P_1P_8\right)+\mathrm{Pr}\,LeKcP_7-\frac{Nt}{Nb}P_6^{'}\right], \tag{24}$$

$$P_{10}^{'}=P_{10}\left(Lb\,\mathrm{Re}\,P_1+Pe\,P_8\right)+Pe\,P_8^{'}\left(P_9+N_\delta\right). \tag{25}$$

with the boundary conditions as

$$\begin{cases} P_1(-1)=0, \\ P_2(-1)=\alpha_1P_4(-1)+2, \\ P_5(-1)=\alpha_2P_6(-1)+1, \\ P_7(-1)=\alpha_3P_8(-1)+1, \\ P_9(-1)=\alpha_4P_{10}(-1)+1 \\ \& \\ P_2(1)=-2\alpha, P_1(1)=0=P_5(1)=P_7(1)=P_9(1). \end{cases} \tag{26}$$

Here, *De* represent the Deborah number, *Re* the stretching Reynolds number, *Pr* the Prandtl number, and *M* the magnetic parameter, *Nr* the buoyancy ratio, λ the mixed convection, *Rd* the thermal radiation, *Nc* the bioconvection Rayleigh number, *Nb* the Brownian motion parameters, *Q* the heat source, *Nt* the thermophoresis parameter, *Sc* the Schmidt number, *Kc* the chemical reaction, and *Le*, *Lb*, *Pe* are the Lewis, the bioconvective Lewis and, the Peclet numbers, N_δ the motile microbes' density difference, λ_2 the thermal time-relaxation Deborah number, λ_3 the concentration time-relaxation Deborah number, γ the stretching ratio parameter of disks, (α_1, α_2, α_3) the velocity, thermal and concentration slips, and α_4 the gyrotactic microorganisms slip. These quantities are defined respectively as

$$\left.\begin{aligned} &De=\lambda_1s_2,\ Re=\frac{s_1h^2}{\nu},\ M=\sqrt{\frac{\beta_0^2\sigma_e}{\rho s_1}}, \\ &Nr=\frac{\left(\rho_p-\rho_f\right)\left(C_1-C_2\right)}{\beta^{**}\rho_f\left(1-C_f\right)\left(T_1-T_2\right)},\ \lambda=\frac{\beta^{**}g\left(1-C_2\right)T_2}{h\left(\rho c\right)_f}, \\ &Rd=\frac{4\sigma T_\infty^3}{kk^*},\ Nc=\frac{\gamma^*\left(\rho_m-\rho_f\right)\left(N_1-N_2\right)}{\rho_f\beta^{**}\left(1-C_2\right)\left(T_1-T_2\right)}, \\ &\mathrm{Pr}=\frac{\mu c_p}{k},\ Nb=\frac{\tau D_B}{\nu}\left(C_1-C_2\right),\ Q=\frac{Q^*}{h\left(\rho c_p\right)_f}, \\ &Nt=\frac{\tau D_T}{\nu T_m}\left(T_1-T_2\right),\ Sc=\frac{\nu}{D_n},\ Kc=\frac{K_r^*}{h},\ Le=\frac{\nu}{D_B}, \\ &Lb=\frac{\nu}{D_m},\ Pe=\frac{bWc}{D_m},\ N_\delta=\frac{N_2}{N_1-N_2}, \\ &\lambda_2=\tau_1s_2,\ \lambda_3=\tau_2s_2,\ \gamma=\frac{s_2}{s_1},\ \alpha_1=\frac{\gamma_1}{h}, \\ &\alpha_2=\frac{\gamma_2}{h},\ \alpha_3=\frac{\gamma_3}{h},\ \alpha_4=\frac{\gamma_4}{h} \end{aligned}\right\} \tag{27}$$

4. Results and Analysis

The implication of several associated parameters of the system on dimensionless velocity (axial, radial), temperature, concentration, and the gyrotactic motile microbes' density fields is the primary focus of this section. For this purpose, Figs. 2(a)-4(f) are induced to analyze the behavior of these productive parameters. The physical ranges of associated constraints are assumed based on the physical importance of these parameters [53, 54]. Here, the two cases that represent the Casson-Maxwell nanofluid flow (CMNF) and Casson nanofluid flow (CNF) are displayed graphically. Table 1 provides a lucid comparison of current findings to those published in the literature, revealing a good match.

Figs. 2(a-b) outline the prominence of the stretching ratio parameter γ on the radial and axial velocities $\left(F'(\zeta),F(\zeta)\right)$ for both fluids, respectively. In Fig. 2(a), the axial velocity escalates against increasing stretching ratio parameter ranges. Physically, the top disk will exhibit more fluid axially, where a greater amount of radially incoming fluid near the fast-spinning disk is thrown out. Hence $F(\zeta)$ boosted up but slightly slower as compared to the Casson fluid. Fig. 2(b) depicts the impression of the stretching ratio on the radial velocity for both fluids. It can be acknowledged that the radial velocity is enhanced near the bottom disk. Physically, the stretching produces more pressure on the surface, which concludes in an upturn of the velocity profile. These velocity profiles are parabolic. Further, the symmetric parabolic profiles are obtained when γ = 1, and hence resemble those in the case of stationary non-stretchable disks [55].

Figs. 2(c-d) reveal how the magnetic parameter *M* behaves on the axial and radial velocities for both fluids, respectively. The upsurge in magnetic parameter values diminished the radial and axial velocities of the two fluids. It can be analyzed from the graphical results that the axial velocity of Casson nanofluid is influenced by *M*

Table 1. A comparative analysis of the local Nusselt number for distinct *Pr* with $\gamma = \lambda = Nr = Nc = Rd = Lb = Pe = 0$.

Pr	Ahmad *et al.* [36]	Shevehuk [43]	Present outcomes
0.41	0.2264970	0.2264	0.226474
0.51	0.262336	0.2624	0.262300
0.61	0.2942853	0.2945	0.294358
0.71	0.3258596	0.3258	0.325861
0.72	0.328573	0.3288	0.328620
0.82	0.3494468	0.3497	0.349446
0.90	0.3737099	0.3739	0.373653
1.0	0.3963238	0.3964	0.396340

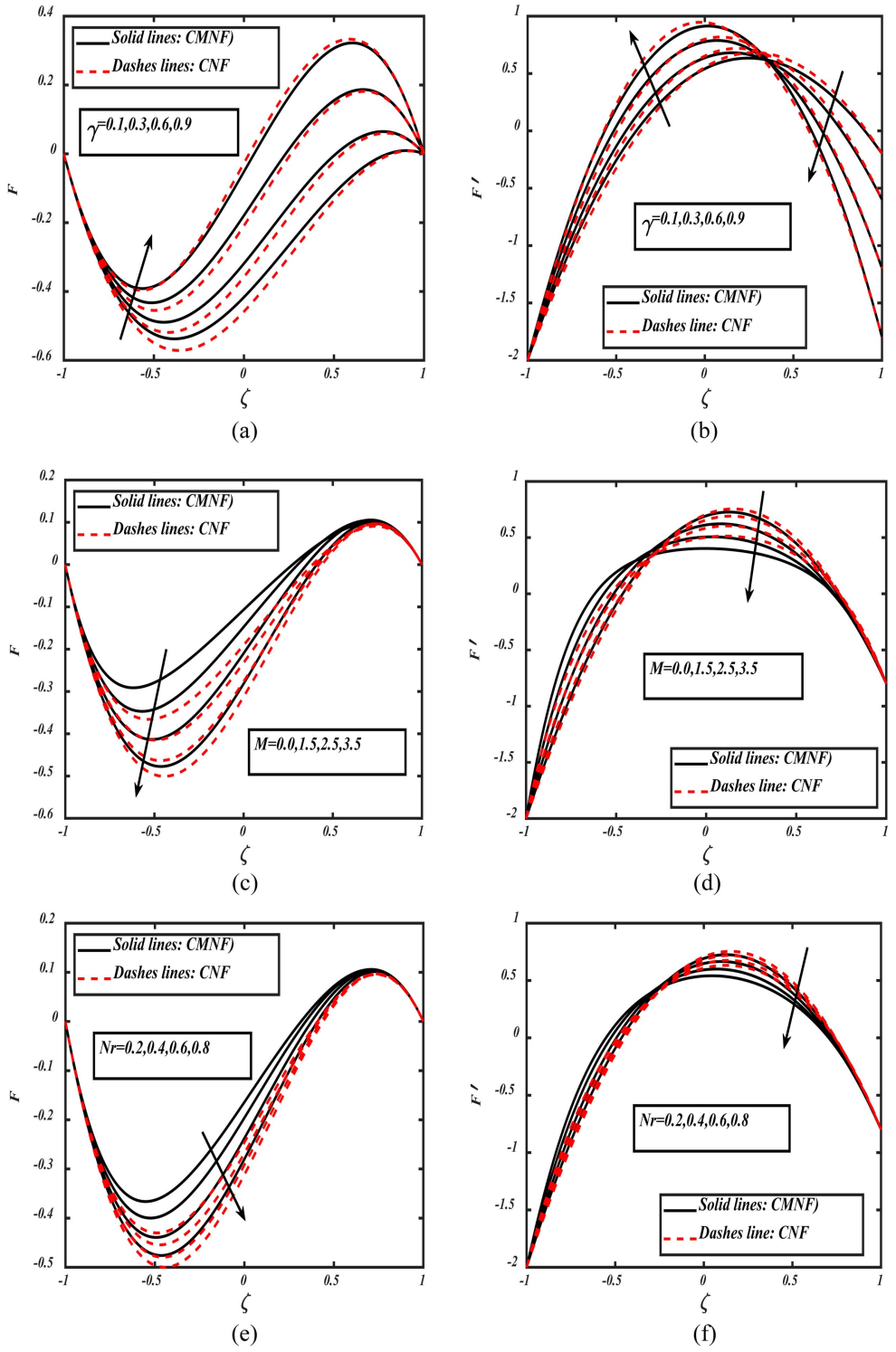


Fig. 2. (Color online) (a) Impression of γ on F, (b) Impression of γ on F', (c) Impression of M on F, (d) Impression of M on F', (e) Impression of Nr on F, (f) Impression of Nr on F'.

more rapidly as compared to the Casson-Maxwell nanofluid and conversely in the case of the radial velocity. The fluid velocities are physically opposed by the resistive force (Lorentz drag force) produced by the magnetic field that acts opposite to the direction of fluid motion.

Figs. 2(e-f), 3(a) elaborate on the behavior of Nr (the buoyancy ratio) and Nc (Rayleigh number for bioconvection) on the axial and radial velocity profiles for both fluids,

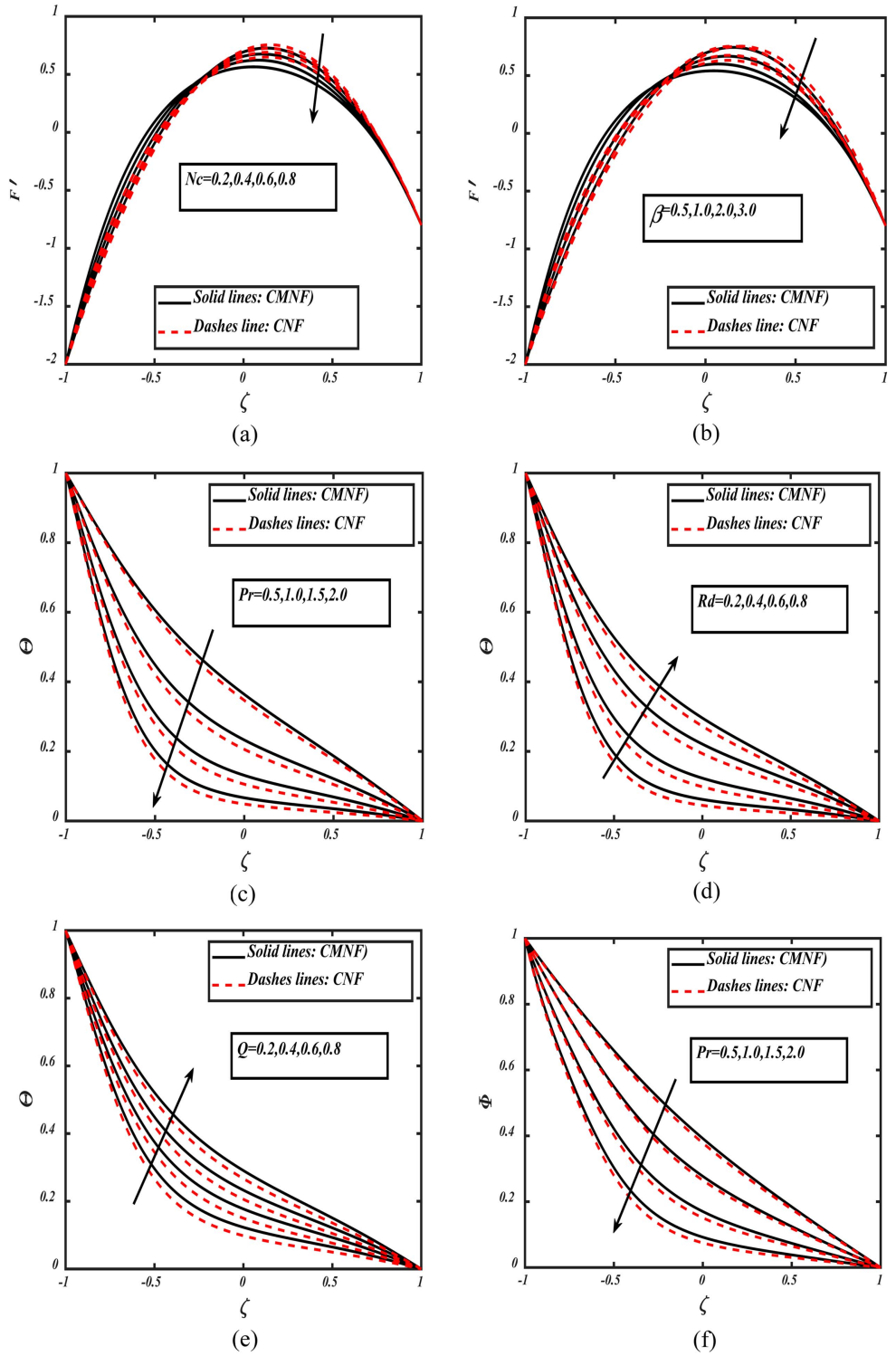


Fig. 3. (Color online) (a) Impression of Nc on F', (b) Impression of β on F', (c) Impression of Pr on θ, (d) Impression of Rd on θ, (e) Impression of Pr on θ, (f) Impression of Pr on ϕ.

respectively. The graphical results show that a depreciation in the velocity profiles can be observed corresponding to the magnifying magnitudes of Nr, and Nc. Physically, for increasing the bioconvection Rayleigh number, the buoyancy force caused by bioconvection results in decreased velocity. The momentum boundary layer becomes thinner, leading to a reduction in the fluid velocity. Therefore, higher values of the bioconvection Rayleigh number weaken the

velocity field due to the intensified bioconvective buoyancy effects.

Fig. 3(b) is considered to argue the contribution of β the Casson fluid parameter on the velocity gradient $F'(\zeta)$ for the two distinct cases of velocity slip α_1. The velocity gradient is de-escalated for higher values of β. Physically, a greater Casson parameter value lowers the yield stress of fluid, therefore it weakens the shear developed at the disk surface. Consequently, the momentum transfer from the stretching disk to the adjacent fluid is reduced, leading to a declined velocity gradient. Further, with the incorporation of a velocity slip constraint, the declination rate is too fast.

Figs. 3(c-e) are illustrated to emphasize the implications of Prandtl number *Pr*, thermal radiation *Rd*, and heat source *Q* on the dimensionless temperature field $\theta(\zeta)$ for both fluids. Fig. 3(c) depicts the variable behavior of $\theta(\zeta)$ against the growing *Pr* magnitudes. The temperature decreases due to weak thermal diffusivity corresponding to increasing *Pr* magnitudes, so the thermal profile behaves as a decreasing function. The rate of declination in the temperature profile is slightly rapid in the Casson nanofluid as compared to the Casson-Maxwell nanofluid. Fig. 3(d) displays that the electromagnetic waves' radiations accelerate the flow streams by increasing fluid particles' kinetic energy and hence elevates the temperature further. However, closer to the surface of the disks, the temperature drops with a greater thermal radiation effect. A comparison between the two fluids (Casson-Maxwell and Casson) under the impact of *Rd* can be discerned from the graph (see Fig. 3(d)). In Fig. 3(e), it can be examined that the augmenting magnitudes of the heat source *Q* comprehensively raise the temperature at all localities between the disks. This feature represents hot spots in the processing of materials that can be harnessed to stimulate heat energy during manufacturing procedures [56].

The Prandtl number *Pr* evaluation on nanomaterials concentration ϕ is deliberated using Fig. 3(f). The enlarging *Pr* magnitudes abate the volumetric concentration profile throughout the boundary layer. Physically, larger values of the Prandtl number correspond to lower thermal diffusivity, which weakens thermal transport within the fluid. Consequently, the coupled heat and mass transfer mechanisms become less effective, leading to a thinner concentration boundary layer and a reduction in the nanoparticle concentration. Fig. 4(a) demonstrates the chemical reaction response through the parameter *Kr*. The nanomaterials' concentration $f(\zeta)$ declines with rising chemical reaction response. Physically, this occurs due to the reduced molecular diffusivity against boosting the chemical reaction parameter, as a result, nanoparticles concentration decreases. The Brownian motion for both fluids against the density field can be examined in Fig. 4(b). For increasing the Brownian motion parameter *Nb*, a diminishing behavior of the concentration field can be observed. The decreasing rate of concentration gradient is slightly rapid for the Casson nanofluid (in the absence of concentration slip parameter α_3). Physically, higher Brownian motion increases the fluid's temperature, and the nanomaterials move away from a hot to a relatively cold region, which brings down the concentration profile as well. It is analyzed in Fig. 4(c); the volumetric concentration is boosted parallel to the boosting thermophoretic parameter *Nt* values in both fluids. Further, the increasing rate is marginally agile for the Casson-Maxwell nanofluid. Physically, particles migrated towards a comparatively low warm region by rising *Nt* values that optimize the nanoparticles' volume fraction $f(\zeta)$.

Fig. 4(d) shows that accretion in the magnetic parameter *M*, maximize the motile microorganisms' density in both fluids. The increasing rate is slightly quicker for the Casson-Maxwell nanofluid in contrast to the Casson nanofluid. Physically, an additional resistive force generated by the magnetic field boosted the motility rate, and hence the motile microbes' density is increased. Fig. 4(e) demonstrates the consequences of bioconvective Peclet number (*Pe*) on the concentration field of gyrotactic microbes $\chi(\zeta)$ of both fluids. The Peclet number of bioconvection has a direct impression on the microorganisms' concentration and hence significantly dominates the concentration of gyrotactic motile microbes. The Peclet number of bioconvection assists in boosting the momentum of motile microbes, and so the microbes' density is declined near the surface. Physically, bioconvection Peclet number represents the ratio of microorganism advection to microorganism diffusion. It determines how microorganisms are transported by the rotating flow. Also, it influences nutrient and oxygen transport in biological systems. It is important for optimizing photobioreactors and fermentation equipment, and controls microorganism dispersion in rotating biological devices. The impression of the microbes' density profile of bioconvection Lewis number *Lb* is argued from Fig. 4(f). A sharp decline in the profile can be noticed as the bioconvective Lewis number resists the fluid stream. For higher *Lb* magnitudes, the diffusivity of microbes' declines, and so does the density. The rate of decrease in $\chi(\zeta)$ (for *Pe* and *Lb*) is barely faster in the Casson-Maxwell nanofluid as compared to the Casson nanofluid. Bioconvection Lewis Number is the ratio of thermal diffusivity to microorganism diffusivity. So, physically, it governs the interaction between heat transfer and microorganism transport. It is important in systems where temperature affects microorganism distribution,

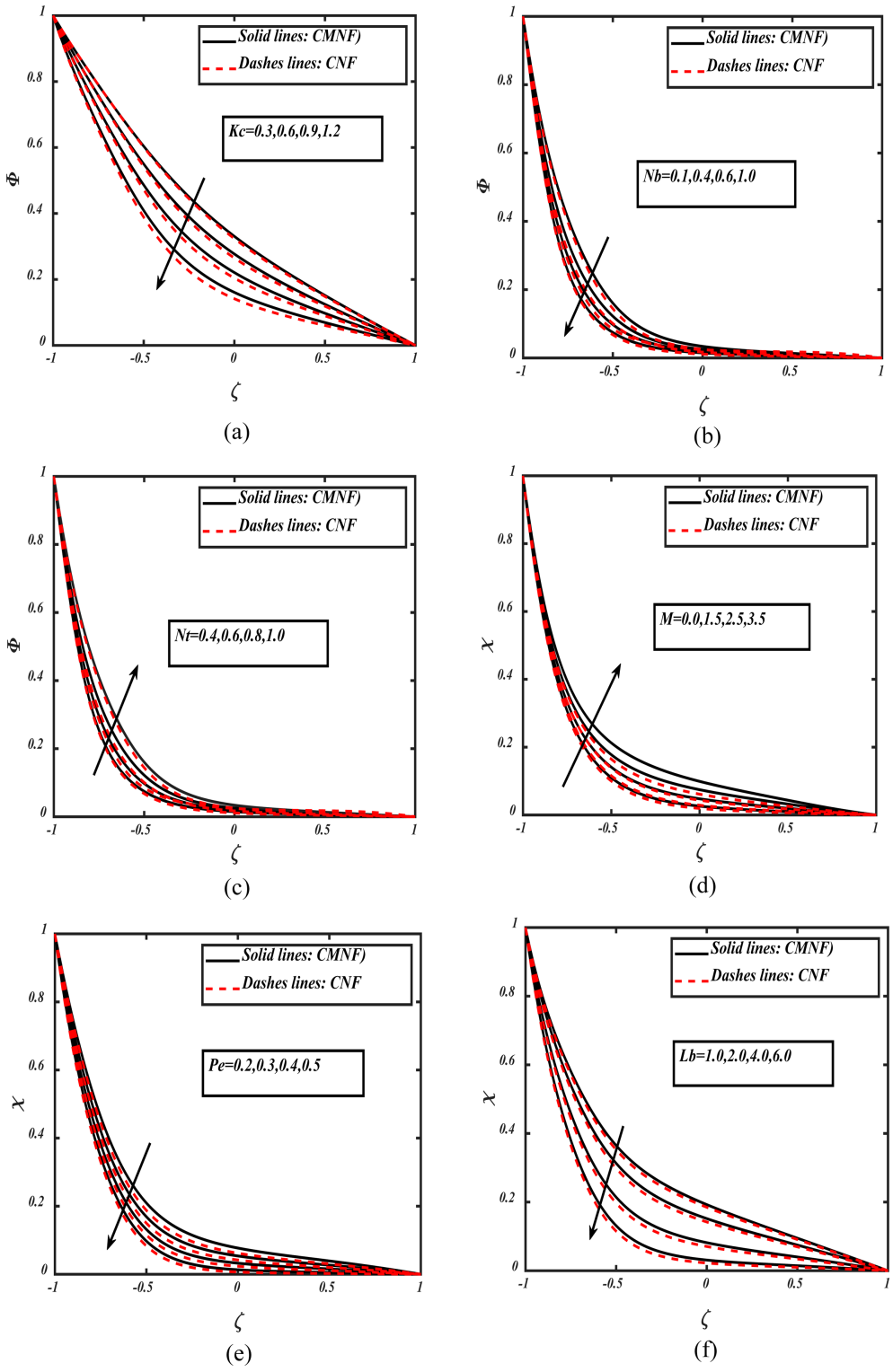


Fig. 4. (Color online) (a) Impression of *Kc* on ϕ, (b) Impression of *Nb* on ϕ, (c) Impression of *Nt* on ϕ, (d) Impression of *M* on χ, (e) Impression of *Pe* on χ, (f) Impression of *Lb* on χ.

relevant to solar bioreactors, biofuel production, and thermal bioprocesses.

To describe the flow behavior adequately, streamlines are drawn for different emerging parameters across the domain of the model (see Figs. 5(a-d). Fig. 5(a) shows that the streamline contours display a smooth and symmetric

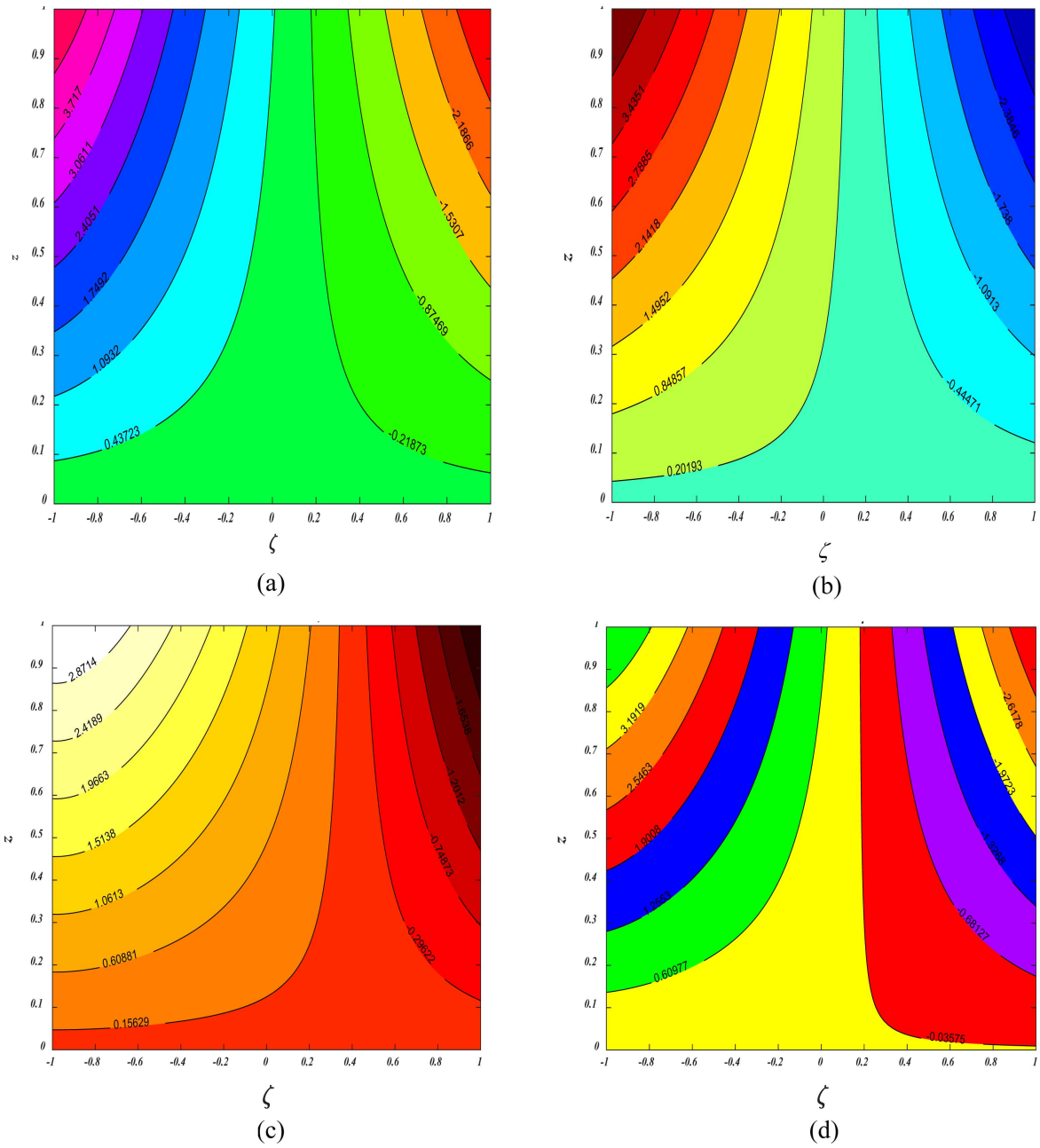


Fig. 5. (Color online) (a) Streamlines for $\beta = De = 0.3$, (b) Streamlines for CNF and MNF = 0, (c) Streamlines when $M = 0.5$ and $\gamma = 0$ for CMNF, (d) Streamlines when $M = 0.5$ and $\gamma = 0.4$ for CMNF.

distribution around the rotating disks, which indicates a stable boundary layer flow. In Fig. 5(b), the comparatively greater spacing between adjacent streamlines portrays a weaker momentum interaction. Fig. 5(c) explains that the magnetic impact compresses the streamline contours towards the disk surface. The Lorentz force retards the motion of nanofluid, suppressing fluid convection and reducing the momentum boundary-layer thickness. Consequently, the flow becomes more ordered and remains free from recirculation. In the absence of Lorentz force (see Fig. 5(d)), disk stretching enhances the transport of fluid away from the surface. Consequently, the streamlines spread further into the flow domain and exhibit greater curvature, indicating stronger convective transport.

5. Conclusions

A three-dimensional, steady, incompressible, and electrically

conductive Casson-Maxwell nanofluid flow across the parallel and stretchable disks implementing the Buongiorno model is analyzed. The present bioconvective nanofluid model further accounts for the influences of thermal radiation, chemical reaction, and heat source effects.

By employing similarity transformations, the governing partial differential equations are reduced to non-dimensional ordinary differential equations. The resulting system is then solved numerically using the bvp4c solver together with the fourth-order Runge–Kutta (RK4) method.

This study clearly demonstrates that the combined effects of yield stress and viscoelasticity produce markedly different transport characteristics in the Casson–Maxwell fluid compared with the Casson fluid. A comparative analysis further discloses that the fluid elasticity changes the response of the flow under magnetic and thermal effects, leading to different momentum and heat transfer characteristics for the Casson–Maxwell fluid. The concluding remarks are summarized as:

- The velocities of both fluids towards axial and radial directions decreases with increasing magnetic effects. The axial velocity of the Casson nanofluid is affected more rapidly by M as compared to the Casson-Maxwell nanofluid, and a contrary pattern is noticed in the case of the radial velocity profile.
- Increasing the Casson fluid parameter changes the intrinsic rheological properties of the fluid by changing its yield stress and effective viscosity, so the velocity profile declines. This declination rate is too fast in the presence of a velocity slip constraint.
- Bioconvection affects the thermal transmission characteristics of the fluid. Particularly, rising bioconvection parameter values change the temperature distribution, that is an increase in local Nusselt number (as calculated in Table 1), which clearly indicates the enhancement of heat transfer.
- The higher magnitudes of the stretching ratio γ boost the fluids' flow as robust disk stretching improves momentum transfer within the boundary layer.
- The accelerating thermal radiation Rd and heat source Q parameter values comprehensively raise the temperature at all localities. The thermal profile of the Casson-Maxwell fluid is boosted rapidly compared to the Casson fluid. The Casson–Maxwell fluid demonstrates a thicker thermal boundary layer than the Casson fluid.
- For larger magnitudes of the Brownian motion Nb parameter, a diminishing behavior of the concentration profile can be observed. The decreasing rate of concentration gradient is slightly rapid for the Casson nanofluid (neglecting the concentration slip α_3 parameter).
- For rising thermophoretic parameter Nt values, the volumetric concentration profile is boosted for both fluids. Further, the increasing rate is marginally agile for Casson-Maxwell nanofluid.
- It is found that aggrandizing the magnetic parameter M values causes the motile microorganisms' profile to be maximized, while a contrary trend is noticed for the bioconvective Peclet and the bioconvective Lewis numbers for both fluids. The rate of decrease in $\chi(\zeta)$ (for Pe and Lb) is marginally faster in the Casson-Maxwell nanofluid as compared to the Casson nanofluid.

These findings provide useful insight into the coupled transport mechanisms in rotating non-Newtonian nanofluids. Potential engineering applications include rotating disk reactors for chemical processing, turbine and gas-engine cooling, magnetic cooling and flow control devices, polymer coating and spin-coating technologies, rotating heat exchangers, nuclear and solar thermal energy systems, electronic cooling of rotating machinery, biomedical centrifugal devices, microbial bioreactors, and wastewater treatment systems. The incorporation of thermal radiation, heat generation, chemical reactions, and bioconvection further extends the applicability of the model to high-temperature manufacturing processes, catalytic reactors, renewable energy technologies, and bio-inspired thermal management systems.

Acknowledgement

The authors extend their appreciation to the Deputyship for Research & Innovation, Ministry of Education in Saudi Arabia for funding this research work through the project number 0038-1446-S.

Funding Statement

This research work was supported by the Ministry of Education–Kingdom of Saudi Arabia [0038-1446-S].

Conflicts of Interest

The authors declare that they have no conflicts of interest to report regarding the present study.

Nomenclature

C Concentration of nanoparticles, $molL^{-1}$
C_f Skin friction coefficient
C_1 Concentration of nanoparticles (at lower disk)
C_2 Concentration of nanoparticles (at lower disk)
u, v, w Velocity vectors

D_B Coefficient of Brownian diffusion, m^2s^{-1}
D_m Microorganisms' diffusivity, m^2s^{-1}
De Deborah number
D_T Coefficient of Thermophoresis diffusion, m^2s^{-1}
Lb Bioconvective Lewis number
Le Bioconvection Lewis Number
N Density of microorganisms, m^{-3}
Nb Brownian diffusion parameter
T_m Mean fluid temperature
Kr Reaction rate constant
M Magnetic parameter
Wc Maximum cell swimming speed
ϕ Dimensionless volume fraction of nanoparticles
ζ Similarity variable
ρ_m Microorganism particles density
$(\rho c)_f$ Heat capacity of base fluid, $Jm^{-3}\ K^{-1}$
λ Mixed convection parameter
λ_1 Time relaxation parameter
λ_2 Deborah number caused by time of thermal relaxation
λ_4 Deborah number caused by time of microorganisms' relaxation
γ^* Average volume of the microorganism
β Casson parameter
k Thermal conductivity
γ_2 Thermal slip coefficient
γ_4 Microorganisms slip coefficient
g Acceleration due to gravity, m^2s^{-1}
τ_1 Heat flow relaxation time
b Chemotaxis constant
s_1 Lower disk stretching rate
N_1 Microorganisms' concentration (at lower disk)
N_2 Microorganisms' concentration (at upper disk)
Pe Bioconvection Peclet number
Pr Prandtl number
W_c Maximum cell swimming speed
C_P Specific heat at constant pressure
Nc bioconvection Rayleigh number
Q Heat sourse
Nr Buoyancy ratio parameter
Rd Thermal radiation parameter
N_δ Microorganisms' concentration difference parameter
Nt *Thermophoresis number*
S_n Microorganisms' density number
T Temperature of fluid, K
Kc Chemical reaction parameter
S Dimensionless heat source
θ Dimensionless temperature
χ Dimensionless microorganisms' density function
ρ_f Density of fluid, kgm^{-3}
$(\rho c)_p$ Heat capacity of nanoparticles, $Jm^{-3}\ K^{-1}$
μ Dynamic viscosity of nanoliquid, Nsm^{-2}
γ Stretching ratio parameter
β^{**} Thermal expansion coefficient
λ_3 Deborah number caused by time of concentration relaxation
σ^* Stefan-Boltzmann constant
p Pressure
β_0 Strength of magnetic field
γ_1 Velocity slip coefficient
γ_3 Concentration slip coefficient
σ_e Electrical conductivity
τ Ratio between heat capacity of nanoparticles and base fluid
τ_2 Mass flux relaxation time
r Radius of disk, m
s_2 Upper disk stretching rate

References

[1] D. Cioranescu, V. Girault, and K. R. Rajagopal, Mechanics and Mathematics of Fluids of the Differential Type, Springer, Cham (2016) pp. 1-394.
[2] S. A. Shehzad, T. Hayat, and A. Alsaedi, Comput. Appl. Math. **37**, 2932 (2018).
[3] M. I. Khan, M. Waqas, T. Hayat, and A. Alsaedi, J. Colloid Interface Sci. **498**, 85 (2017).
[4] U. Farooq, M. A. Ijaz, M. I. Khan, S. S. P. M. Isa, and D. C. Lu, Int. Commun. Heat Mass Transf. **119**, 104955 (2020).
[5] M. Sohail, Z. Shah, A. Tassaddiq, P. Kumam, and P. Roy, Sci. Rep. **10**, 12530 (2020).
[6] S. Rashid, M. I. Khan, T. Hayat, M. Ayub, and A. Alsaedi, Appl. Nanosci. **10**, 2965 (2020).
[7] M. Khan, J. Ahmed, and W. Ali, J. Therm. Anal. Calorim. **143**, 4081 (2021).
[8] S. A. Shehzad, F. Mabood, A. Rauf, and I. Tlili, Int. Commun. Heat Mass Transf. **116**, 104693 (2020).
[9] H. Waqas, M. Imran, and M. M. Bhatti, Chin. J. Phys. **68**, 558 (2020).
[10] R. P. Gowda, R. N. Kumar, A. Aldalbahi, A. Issakhov, B. C. Prasannakumara, M. Rahimi-Gorji, and M. Rahaman, Surf. Interfaces **22**, 100864 (2021).
[11] P. G. R. Jayadevamurthy, N. K. Rangaswamy, B. C. Prasannakumara, and K. S. Nisar, Numer. Methods Partial Differ. Equ. **40**, 22680 (2024).
[12] M. Turkyilmazoglu, Int. J. Eng. Sci. **51**, 233 (2012).
[13] J. Ahmed, M. Khan, and L. Ahmad, Chin. J. Phys. **60**, 22 (2019).
[14] S. U. Choi and J. A. Eastman, Enhancing Thermal Conductivity of Fluids with Nanoparticles, No. ANL/MSD/CP-84938; CONF-951135-29, Argonne National Laboratory, Argonne, IL (1995) pp. 99-105.
[15] J. Buongiorno, J. Heat Transfer **128**, 240 (2006).
[16] M. Turkyilmazoglu, Eur. J. Mech. B Fluids **53**, 272 (2015).
[17] O. Pourmehran, M. Rahimi-Gorji, M. Hatami, S. A. R.

Sahebi, and G. Domairry, J. Taiwan Inst. Chem. Eng. **55**, 49 (2015).
[18] M. Hatami, D. Song, and D. Jing, Int. J. Heat Mass Transf. **98**, 758 (2016).
[19] S. Nadeem, R. Ul Haq, N. S. Akbar, C. Lee, and Z. H. Khan, PLoS One **8**, e69811 (2013).
[20] A. A. Afify and M. A. El-Aziz, Pramana **88**, 31 (2017).
[21] C. Yang, W. Li, and A. Nakayama, Int. J. Therm. Sci. **71**, 249 (2013).
[22] T. Hayat, A. Nassem, M. I. Khan, M. Farooq, and A. Al-Saedi, Phys. Chem. Liq. **56**, 189 (2018).
[23] M. I. Khan, F. Alzahrani, A. Hobiny, and Z. Ali, J. Mater. Res. Technol. **9**, 6172 (2020).
[24] S. Qayyum, M. I. Khan, W. Chammam, W. A. Khan, Z. Ali, and W. Ul-Haq, Mod. Phys. Lett. B **34**, 2050383 (2020).
[25] M. Gnaneswara Reddy, R. J. Punith Gowda, R. Naveen Kumar, B. C. Prasannakumara, and K. Ganesh Kumar, Proc. Inst. Mech. Eng. Part E: J. Process Mech. Eng. **235**, 1259 (2021).
[26] A. V. Kuznetsov, Int. Commun. Heat Mass Transf. **37**, 1421 (2010).
[27] S. U. Khan and H. M. Ali, Int. J. Thermophys. **41**, 1 (2020).
[28] Y. M. Chu, S. Aziz, M. I. Khan, S. U. Khan, M. Nazeer, I. Ahmad, and I. Tlili, Phys. Scr. **95**, 105007 (2020).
[29] S. U. Khan, K. Al-Khaled, and M. M. Bhatti, Surf. Interfaces **23**, 100982 (2021).
[30] M. Ramzan, J. D. Chung, and N. Ullah, Int. J. Mech. Sci. **130**, 31 (2017).
[31] S. A. Shehzad, T. Mushtaq, Z. Abbas, A. Rauf, S. U. Khan, and I. Tlili, Appl. Math. Mech. **41**, 1333 (2020).
[32] F. Tuz Zohra, M. J. Uddin, M. F. Basir, and A. I. M. Ismail, Proc. Inst. Mech. Eng. Part N. J. Nanomater. Nanoeng. Nanosyst. **234**, 83 (2020).
[33] M. I. Khan, H. Waqas, S. U. Khan, M. Imran, Y. M. Chu, A. Abbasi, and S. Kadry, Int. Commun. Heat Mass Transf. **122**, 105161 (2021).
[34] S. Nadeem, M. Ijaz, A. El-Kott, and M. Ayub, Ain Shams Eng. J. **11**, 1295 (2020).
[35] M. Ramachandru, D. Hymavathi, M. Chenna Krishna Reddy, M. Fareeduddin, N. Kishan, M. Umeshaiah, and H. S. Gill, Int. J. Mod. Phys. B **37**, 2350300 (2023).
[36] Z. Uddin, H. Upreti, S. Ganga, and W. Ibrahim, Sci. Rep. **14**, 7891 (2024).
[37] O. A. Bég, U. I. Usman, T. A. Bég, M. M. Channakote, H. J. Leonard, and M. M. Bhatti, J. Comput. Appl. Mech. **57**, 369 (2026).
[38] M. M. Bhatti, J. Comput. Appl. Mech. **57**, 443 (2026).
[39] Z. Asghar, M. W. S. Khan, M. A. Gondal, and A. Ghaffari, Proc. Inst. Mech. Eng. Part E: J. Process Mech. Eng. **239**, 87 (2025).
[40] M. Waqas, Z. Asghar, and W. A. Khan, Eur. Phys. J. Spec. Top. **230**, 1307 (2021).
[41] Z. Asghar, M. W. S. Khan, A. Alhashash, and M. A. Gondal, Chin. J. Phys. **95**, 455 (2025).
[42] R. Ellahi, A. Zeeshan, N. Shehzad, A. Hussain, and S. M. Sait, Nanotechnology **35**, 095402 (2024).
[43] J. Mehboob, R. Ellahi, S. M. Sait, and N. S. Akbar, Int. J. Numer. Methods Heat Fluid Flow **35**, 825 (2025).
[44] S. Z. Alamri, A. A. Khan, I. Nasreen, and R. Ellahi, J. Comput. Appl. Mech. **56**, 776 (2025).
[45] A. Ali, M. Umar, Z. Bukhari, and Z. Abbas, Results Phys. **19**, 103544 (2020).
[46] J. Ahmed, M. Khan, and L. Ahmad, Chin. J. Phys. **60**, 22 (2019).
[47] T. Hayat, S. Qayyum, M. Imtiaz, and A. Alsaedi, Results Phys. **7**, 126 (2017).
[48] Z. Abbas, T. Mushtaq, S. A. Shehzad, A. Rauf, and R. Kumar, J. Braz. Soc. Mech. Sci. Eng. **41**, 1 (2019).
[49] J. Mehboob, R. Ellahi, and S. M. Sait. Symmetry **16**, 717 (2024).
[50] M. S. Kumar, N. Sandeep, B. R. Kumar, and S. Saleem, Alex. Eng. J. **57**, 2027 (2018).
[51] M. M. Hashmi, T. Hayat, and A. Alsaedi, Nonlinear Anal. Model. Control **17**, 418 (2012).
[52] K. Ali, S. Ahmad, and M. Ashraf, Therm. Sci. **21**, 2155 (2017).
[53] I. V. Shevchuk, Convective Heat and Mass Transfer in Rotating Disk Systems, Vol. **45**, Springer, Berlin (2009) pp. 1-36.
[54] M. Turkyilmazoglu, Mediterr. J. Math. **13**, 4019 (2016).
[55] K. Ali, S. Ahmad, and M. Ashraf, Therm. Sci. **21**, 2155 (2017).
[56] E. P. Douglas, Materials Processing in Magnetic Fields (2005) pp. 310-320.